Nonlinear Dyn
https://doi.org/10.1007/s11071-024-10679-8

RESEARCH

Cantilevers attached with bluff bodies: vortex-induced vibrations

Khawar Zamman Wani · Manoj Pandey · Balakumar Balachandran

Received: 27 June 2024 / Accepted: 17 November 2024

Abstract Vortex-induced vibrations are oscillatory motions experienced by a body interacting with an external flow. These vibrations can be harnessed for energy harvesting purpose. A cantilever beam with a cylinder attached at the free end represents the bluff-body oscillator of interest here. Vortex-induced vibrations of two adjacent bluff-body oscillators are studied by varying the transverse spacing between the oscillators. A finite element model of the system is used to numerically study the associated fluid–structure interactions. For the case with two oscillators, the effect of varying the oscillator spacing on the system response is studied. Dynamic mode decomposition is used for extracting coherent spatio-temporal structures in pressure fields. The system spectral response for the single oscillator and coupled oscillators cases are studied to examine the system dynamics. The obtained numerical results for the system dynamics are found to agree with previously reported experimental results in the literature. The present work can form a basis for constructing computational models of fluid coupled bluff-body oscillators and configuring arrays of bluff-body oscillators for energy harvesting.

Keywords Vortex-induced vibrations · Fluid–structure interactions · Dynamic mode decomposition

List of symbols

A_m^*	Mean nondimensional peak-to-peak amplitude
D	Diameter of the cylinder
f_s	Vortex shedding frequency
g^*	Nondimensional gap
St	Strouhal number
U_0	Flow speed
ALE	Arbitrary Lagrangian Eulerian
CFL	Courant–Friedrichs–Lewy
DMD	Dynamic mode decomposition
FEM	Finite element method
FSI	Fluid–structure interaction
MSE	Mean squared error
POD	Proper orthogonal decomposition
PSD	Power spectral density

1 Introduction

Vortex-induced vibrations (VIVs) are a common phenomenon observed in nature. At external flow speeds higher than a critical value, vortices are shed from the

K. Z. Wani · M. Pandey
Department of Mechanical Engineering, Indian Institute of Technology Madras, Chennai, Tamil Nadu 600036, India
e-mail: khawar@smail.iitm.ac.in

M. Pandey
e-mail: mpandey@smail.iitm.ac.in

B. Balachandran (✉)
Department of Mechanical Engineering, University of Maryland, College Park, MD 20742, USA
e-mail: balab@umd.edu

considered bluff body into the wake behind it. These vortices are shed alternately from each side of the structure, forming a von Kármán vortex street. Vortex shedding is dependent on the Reynolds number (Re) and the geometry and orientation of the bluff body. The shedding frequency is related to a dimensionless number called the Strouhal number (St), which is given by

$$St = \frac{f_s L}{U_0} \tag{1}$$

where f_s is the frequency of vortex shedding, L is a characteristic length, and U_0 is the flow speed. These vortices create fluctuations in the pressure distribution along the surface of the structure, leading to the development of lift forces, resulting in motions transverse to the flow direction. Such fluctuating pressure can also be observed on thin, flexible structures, such as a beam placed in the wake of a cylindrical body, resulting in vortex-induced vibrations of the structure.

Structures in flows can experience vortex-induced vibrations and galloping vibrations. For galloping vibrations, one representative work is that of Luongo et al. [1]. When subjected to vortex-induced vibrations, structures can experience various types of responses, including limit cycle oscillations, chaos, and qualitative changes in behavior due to bifurcations [2–6]. In many engineering applications, these vibrations are undesirable. In civil and aerospace applications, vortex-induced vibrations can lead to structural failures, examples of which include failures of bridges, offshore platforms, and chimneys. On the other hand, these vibrations can be used for energy harvesting purposes by converting the associated mechanical energy into electrical form by using suitable energy transduction mechanisms based on active materials such as the piezoelectric materials.

Two circular cylinders placed side by side in a fluid flow are known to experience rich dynamics. In this regard, the reviews of Sumner [7] and Zhou and Alam [8] are valuable references. The flow physics is strongly dependent on the Reynolds number (Re) and transverse gap-to-diameter ratio (g^*). For $g^* > 1$, two distinct vortex streets are produced [9]. For $g^* > 5$, the two vortex streets are virtually independent of each other. In the regime $1 < g^* < 5$, these vortex streets are coupled, have a single frequency [10], and a definite phase relationship [11]. The vortex streets are synchronized to be either in-phase or anti-phase [12]. By "in-phase," it is meant that these vortices are shed from the corresponding sides of both cylinders simultaneously, while by "anti-phase," it is meant that these vortices are shed from opposite sides of the cylinders at the same time. Synchronization is predominantly found to have an anti-phase character. The frequency of vortex shedding is the same as that of a single isolated cylinder. As the gap is decreased to intermediate values ($0.2 < g^* < 1$), the interactions between the wakes are found to get stronger. The gap flow is deflected, may flip-flop in direction, and is bistable. Two wakes are formed, one narrow and the other wide. The vortex shedding frequency in the narrow wake is approximately three times that of the wide wake [13,14]. For $g^* < 0.2$, vortices are shed only from the free-stream sides of the two cylinders. The shed vortices form a single vortex street. There is no vortex shedding in the gap between the cylinders due to the near wall effect [15].

Bai et al. [16] used the Lattice Boltzmann method for simulations and Dynamic Mode Decomposition (DMD) to identify the spatiotemporal coherent structures present in the flow over two side-by-side cylinders. DMD analysis was carried out for the vorticity field. The authors identified a mean mode M_0 corresponding to steady base flow, the vortex shedding mode M_1, and a secondary mode M_s that corresponds to the gap flow. The corresponding nondimensional frequencies are f_0^*, f_1^*, and f_s^*, respectively. They also observed tertiary modes with nondimensional frequencies $f_1^* \pm f_s^*$. They concluded that the secondary mode M_s contribution to the drag coefficient is much greater than that of the vortex shedding mode M_1, even though the energy of mode M_1 is two orders of magnitude larger than that of mode M_s.

Interactions between the fluid motion and structural motion can also affect the vortex shedding dynamics [17]. These interactions may enable vortex shedding at a Reynolds number smaller than the critical Reynolds number for vortex shedding, as demonstrated in earlier work [18,19] or may suppress this vortex shedding. The flow-induced vibrations of a splitter plate or beam in the wake of a circular cylinder are more complicated than those of circular cylinders because the plate or a beam structure is spatially continuous and has infinite modes of vibration. Additionally, a sufficiently long splitter plate attached to a bluff body such as a cylinder can stabilize the wake and suppress vortex shedding, as demonstrated by Roshko [20]. Kwon and Choi [21] conducted numerical studies on cylinders with attached splitter plates and concluded that with an increase in the splitter plate length, there is a decrease in the Strouhal number. Beyond a critical splitter plate length, no vortex shedding was found to occur for a particular Re.

Akaydin et al. [22] designed and experimentally studied the performance of an energy harvester, called there-in as a linear enegery harvester, consisting of a piezoelectric cantilever beam vibrating in the wake of a stationary cylindrical bluff body. However, the harvester was found to exhibit large-amplitude oscillations only in a narrow range of flow speeds. The same authors designed an enhanced so-called nonlinear energy harvester by attaching a cylindrical bluff body to the tip of the cantilever beam [23]. This resulted in large-amplitude oscillations over a much wider flow speed range as well as an amplified response. Dai et al. [24] developed a reduced-order model for the nonlinear energy harvester design developed by Akaydin et al. [23]. The fluctuating lift on the cylinder was modeled as a van der Pol oscillator by using the wake oscillator model developed by Facchinetti et al. [25]. The harvester was modeled as a forced Euler beam with a tip mass, and a reduced-order model was obtained through Galerkin projection of the governing equations on the dominant linear eigenmodes. In a related recent work by Bellei and Balachandran [26], the authors model the harvester as a geometrically nonlinear piezoelastic beam by using the finite element method and couple this system to a wake oscillator based model for lift. The results have been compared with experimental measurements in the *lock-in* region.

Azadeh-Ranjbar et al. [27] experimentally compared the performance of the linear and nonlinear fluid energy harvesters developed by Akaydin et al. [23], as well as an array of two side-by-side nonlinear fluid energy harvesters in a cross flow. The array with nonlinear harvesters was found to have a significantly larger power output and a wider operating speed range compared to the other cases. This improved result is due to the flow interactions based coupling between the two oscillators. In the same study, Azadeh-Ranjbar et al. presented experimentally obtained information on the energy harvested in the two-oscillator case for different values of the gap-to-diameter ratio g^*. For large g^*, the oscillators behaved like independent harvesters. However, for a small g^* ratio, the authors noticed an increase in the operational speed range and a large maximum power output (approximately ten times for $g^* \approx 0$) compared to that of an isolated harvester.

For various configurations of the oscillators, one will have different flow interactions. By varying the inter-oscillator coupling, one can possibly have a higher energy harvesting for optimal configurations. A robust computational model can help one carry out a parameter optimization analysis. However, no such existing model for a coupled bluff-body oscillator system has been found in the literature. Even for the single oscillator case, a model that is independent of experimental data based parameter fitting is not available. In this work, the authors address this research gap by presenting a finite element model (FEM) for fluid–structure interactions. The computational model can be used to study the responses of the single and coupled nonlinear oscillator cases. The results obtained in the current work are benchmarked by using the experimental results presented by Azadeh-Ranjbar et al. [27].

The rest of the paper is organized as follows. In the next section and Appendices A and B, the computational model developed for studying fluid–structure interactions associated with cantilevers attached with cylindrical bodies are developed. Details of the fluid model, oscillator model, and the methodology used to study fluid–structure interactions are provided in this section along with those for the DMD and POD analysis. The results obtained for the single and two oscillator cases are presented in Sect. 3 and discussed. These results include spectral plots, vorticity contours, POD modes, and DMD modes. In the two oscillator case, the vertical spacing between the oscillators is used as a control parameter and the resulting qualitative changes are examined. Finally, closing remarks are included.

2 Computational modeling

2.1 Finite element model

As an extension of the authors' prior work reported in Wani et al. [28], the Abaqus finite element software [29] is used to model and simulate the fluid–structure interactions associated with the system. The FSI methodology is explained in Appendix A. Alternatives to the FSI methodology presented here include those based on co-simulators (e.g., Roccia et al. [30]).

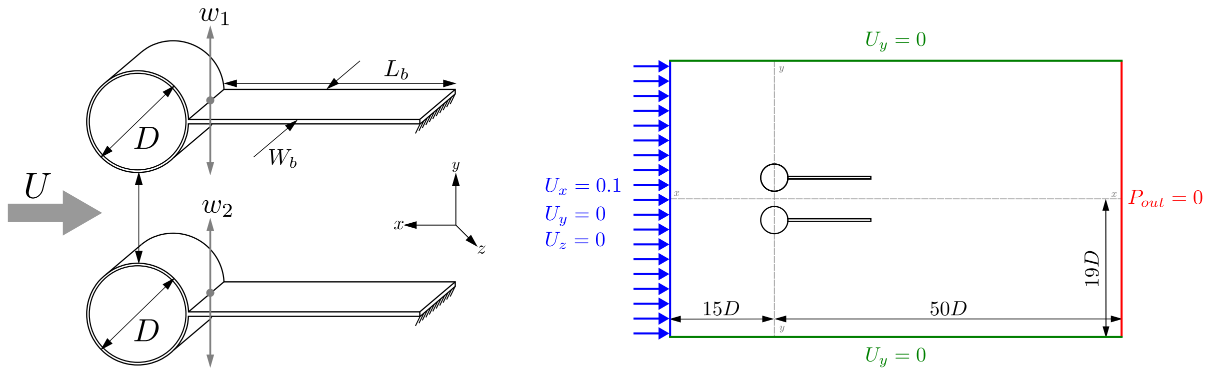

(a) Oscillators in side by side configuration

(b) Fluid domain

Fig. 1 System schematic

2.1.1 Oscillator model

Each oscillator, shown in Fig. 1a, consists of a cantilever beam made of aluminum with a rigid cylinder attached to the beam's free end.

The beam material is modeled as a Saint Venant-Kirchoff material with the constitutive relation:

$$\boldsymbol{S} = \lambda \, \mathrm{tr}(\boldsymbol{E})\boldsymbol{I} + 2\mu \boldsymbol{E} \tag{2}$$

where $\boldsymbol{S}$ is the second Piola-Kirchoff stress tensor, $\boldsymbol{E}$ is the Green-Lagrange strain tensor, λ and μ are Lamé constants and $\boldsymbol{I}$ is the second-order unit tensor. A two-dimensional approximation is used here, and the oscillator is restricted to vibrate in the $x - y$ plane. The parameters of the oscillator model are given in Table 1. The structure is modeled by using C3D8R elements in Abaqus, which are linear hexahedral elements with reduced integration (one integration point). The finite element mesh details are discussed in Appendix B. It is noted that structural models can also be constructed by using other means, for example, see the work of Luongo and Zulli [31].

2.1.2 Fluid domain

The fluid (air) is assumed to be incompressible. The fluid domain, which is shown in Fig. 1b, is rectangular and extends from $-15D$ to $50D$ in the $x-$direction and $-19D$ to $19D$ in the $y-$direction. The boundaries are at least $15D$ away from the fluid–structure interaction (FSI) interface to avoid boundary effects. The centers of the cylinders lie on the transverse axis (y-axis), and are symmetrically arranged about the longitudinal axis (x-axis). The fluid entry into the domain is along the normal to the inlet boundary on the left and the fluid discharge is done at zero pressure through the outlet on the right. Symmetry boundary conditions, $U_y = 0$, are enforced on the upper ($y = 19D$) and lower ($y = -19D$) walls of the domain. To enforce the 2D approximation, the out-of-plane components (i.e., the z component) of displacement and velocity are constrained to be zero. The fluid has a density $\rho_0 = 1.168\,\mathrm{kg\,m^{-3}}$ and viscosity $\mu = 1.800 \times 10^{-5}\,\mathrm{m^2 s^{-1}}$. The fluid domain is discretized by using F3D8R elements in Abaqus, which are linear hexahedral elements with reduced integration. A fluid flow speed $U_0 = 0.10\,\mathrm{ms^{-1}}$, which corresponds to $Re \approx 270$, is used in the simulations. The choice for a low Re is due to the fact that the 2D flow assumption is not valid at high Re [12]. The

Table 1 Model parameters [27]

	Beam	Cylinder
Length L_b, L_c	270.00 mm	32.00 mm
Width W_b	32.00 mm	–
Thickness t_b	0.635 mm	–
Diameter D	–	42.00 mm (outer), 40.00 mm (inner)
Mass Density ρ_b, ρ_c	$2730.00\,\mathrm{kg\,m^{-3}}$	$3640.00\,\mathrm{kg\,m^{-3}}$
Mass m_b, m_c	15.00 g	15.00 g
Young's Modulus E_b, E_c	73.00 GPa	∞
Polar Moment of Inertia J_c	–	$2.205 \times 10^{-6}\,\mathrm{kg\,m^2}$

mesh details as well as the simulation parameters and convergence study results are given in Appendix B.

2.2 DMD and POD analysis

Modal decomposition methods, Proper Orthogonal Decomposition (POD), and Dynamic Mode Decomposition (DMD) are considered to identify the flow's characteristic features. The Proper Orthogonal Decomposition algorithm was introduced in fluid dynamics by Lumley [32]. By carrying out the POD, one identifies the principal modes in the response of a dynamical system that are optimal in terms of capturing the total system energy. The response data can be obtained by sampling and processing information such as the velocity or vorticity fields in fluid mechanics. These modes can be obtained as eigenfunctions of the covariance matrix. These eigenfunctions can be efficiently determined by carrying out the Singular Value Decomposition (SVD) of the snapshot matrix, which is compiled from the response data. By using POD, one can describe the response in terms of a minimum number of modes determined from the response data. The modes are orthogonal; that is, for any two modes ϕ_i and ϕ_j, one has

$$\langle \boldsymbol{\phi}_i, \boldsymbol{\phi}_j \rangle \equiv \int_V \boldsymbol{\phi}_i \cdot \boldsymbol{\phi}_j \, \mathrm{d}V = \delta_{ij}, \quad i, j = 1, \ldots, n \tag{3}$$

The steps to determine the POD modes from the fluid domain data are presented as Algorithm 1.

Algorithm 1 POD

```
Input: Snapshots ${\boldsymbol{x}_k}_{k=1}^N$ where $\boldsymbol{x}_k$ is the state of the system at $k^{\text{th}}$ time instant
Output: POD modes $\boldsymbol{\phi}_j$ with the corresponding eigenvalues $\lambda_j$
Construct data matrix $\boldsymbol{X}$ from snapshots, where $\boldsymbol{X} = [\boldsymbol{x}_1, \boldsymbol{x}_2, \ldots, \boldsymbol{x}_N]$
Compute the mean snapshot $\bar{\boldsymbol{x}}$ and subtract it from all snapshots, creating a zero mean matrix $\tilde{\boldsymbol{X}}$
Compute the Singular Value Decomposition (SVD) of $\tilde{\boldsymbol{X}}$, resulting in $\tilde{\boldsymbol{X}} = \boldsymbol{U}\boldsymbol{\Sigma}\boldsymbol{V}^\top$
Truncate the SVD to rank $r$ by selecting the first $r$ columns of $\boldsymbol{U}$ and first $r$ rows of $\boldsymbol{V}$ and the top-left $r \times r$ submatrix of $\boldsymbol{\Sigma}$, yielding $\boldsymbol{U}_r$, $\boldsymbol{\Sigma}_r$, and $\boldsymbol{V}_r$
The columns of $\boldsymbol{U}_r$ are the POD modes arranged in decreasing order of energy and the diagonal elements of the matrix $\boldsymbol{\Sigma}_r$ are the square roots of the eigenvalues $\lambda_j$. The rows of $\boldsymbol{V}_r$ contain the time history information.
```

Dynamic Mode Decomposition (DMD) is used to approximate the observed temporal evolution of a dynamical system with a close approximation in the form of an autonomous linear dynamical system. Initially proposed by Schmid [33], DMD is based on the Koopman Operator theory. With the Koopman Operator framework, a nonlinear dynamical system is approximated by an infinite-dimensional linear system described by an operator (Koopman Operator), based on the observed data. From the spectral representation of the Koopman Operator, one determines the eigenfunctions that correspond to spatially correlated structures exhibiting consistent temporal behavior. With DMD, one approximates the Koopman decomposition, making it computationally feasible through the use of Singular Value Decomposition (SVD). This process enables one to decompose time-resolved data into modes, where each mode is characterized by a specific frequency and a growth or decay rate. In this study, the Exact DMD algorithm proposed by Tu et al. [34] is employed. With this algorithm, one refines the standard DMD approach to enhance accuracy and robustness. The steps involved in the algorithm are presented as Algorithm 2.

Algorithm 2 Exact DMD

```
Input: Snapshots ${\boldsymbol{x}_k}_{k=1}^N$ where $\boldsymbol{x}_k$ is the state of the system at $k^{\text{th}}$ time instant
Output: DMD modes $\boldsymbol{v}_j$ and discrete time eigenvalues $\mu_j$
Construct data matrices $\boldsymbol{X}$ and $\boldsymbol{X}'$ from snapshot pairs, where $\boldsymbol{X} = [\boldsymbol{x}_1, \boldsymbol{x}_2, \ldots, \boldsymbol{x}_{N-1}]$ and $\boldsymbol{X}' = [\boldsymbol{x}_2, \boldsymbol{x}_3 \ldots, \boldsymbol{x}_N]$.
Compute the Singular Value Decomposition (SVD) of $\boldsymbol{X}$, resulting in $\boldsymbol{X} = \boldsymbol{U}\boldsymbol{\Sigma}\boldsymbol{V}^\top$
Optionally truncate the SVD to rank $r$ by selecting the first $r$ columns of $\boldsymbol{U}$ and $\boldsymbol{V}$ and the top-left $r \times r$ submatrix of $\boldsymbol{\Sigma}$, yielding $\boldsymbol{U}_r$, $\boldsymbol{\Sigma}_r$, and $\boldsymbol{V}_r$
Form the reduced approximation $\tilde{\boldsymbol{A}}$ of the dynamical system by calculating $\tilde{\boldsymbol{A}} = \boldsymbol{U}_r^\top \boldsymbol{X}' \boldsymbol{V}_r \boldsymbol{\Sigma}_r^{-1}$, which corresponds to the projected dynamics in the lower-dimensional space
Solve the eigenvalue problem $\tilde{\boldsymbol{A}}\tilde{\boldsymbol{v}}_j = \mu_j \tilde{\boldsymbol{v}}_j$ to find the discrete time eigenvalues $\mu_j$ and the corresponding eigenvectors $\tilde{\boldsymbol{v}}_j$ of $\tilde{\boldsymbol{A}}$. Each eigenvalue $\mu_j$ is associated with a particular mode $\boldsymbol{v}_j$ of the dynamical system.
Calculate the DMD modes $\boldsymbol{v}_j$ in the original high-dimensional space by projecting the eigenvectors $\tilde{\boldsymbol{v}}_j$ back, using the relation $\boldsymbol{v}_j = \mu_j^{-1} \boldsymbol{X}' \boldsymbol{V}_r \boldsymbol{\Sigma}_r^{-1} \tilde{\boldsymbol{v}}_j$
```

In this work, the package `pyDMD` [35] is used for computing the dynamic mode decomposition of the pressure fields. The mode amplitudes α_i are computed,

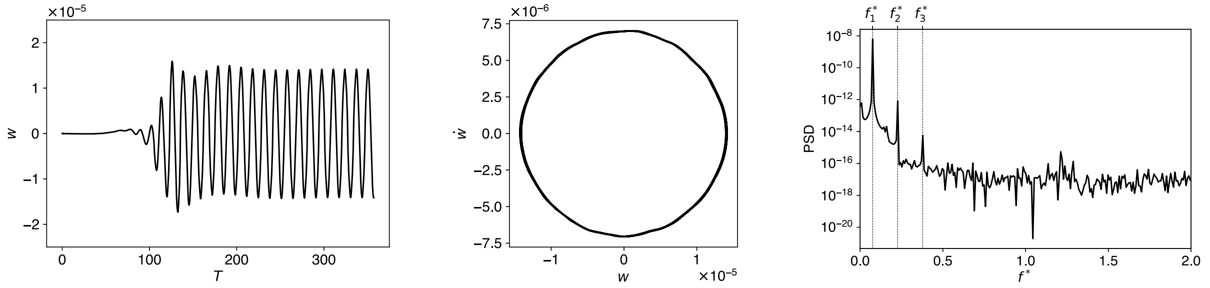

(a) Time history (b) Phase Portrait (c) Power Spectral Density

Fig. 2 Response of a single oscillator

and the dominant modes are chosen. The frequencies are computed from the eigenvalues μ_i.

3 Results

3.1 Nondimensionalization

The displacement and velocity responses are nondimensionalized by dividing them with D and U_0, respectively, where D is the diameter of the cylinder and U_0 is the flow speed. The nondimensionalized frequency f^* is defined as $f^* = 1/T$ where T is the nondimensionalized time given by $T = T'U_0/D$ with T' being the simulation time.

3.2 Single oscillator

In Fig. 2, the displacement response of the cylinder end of the oscillator obtained from the finite element simulations has been plotted. In a previous work of the authors [28], this response was compared with results obtained from the reduced-order model proposed by Dai et al. [24], and a good match was noted. The vortex shedding frequency is determined by taking the PSD of the vorticity magnitude at multiple nodes in the near wake. The vortex shedding frequency is measured to be $f_{vs}^* = 0.0755$. The natural frequency of the oscillator is 18.41 rad s^{-1}. This value corresponds to $f^* = 1.23$ obtained through modal analysis with the finite element model and is found to match the experimentally determined frequency [27]. Hence, the system is operating away from the *lock-in* region. By analyzing the frequency response as shown in Fig. 2c, it can be seen that the response consists of a fundamental frequency $f_1^* = 0.0755$ and odd harmonics of the fundamental frequency $f_2^* = 3f_1^*$ and $f_3^* = 5f_1^*$.

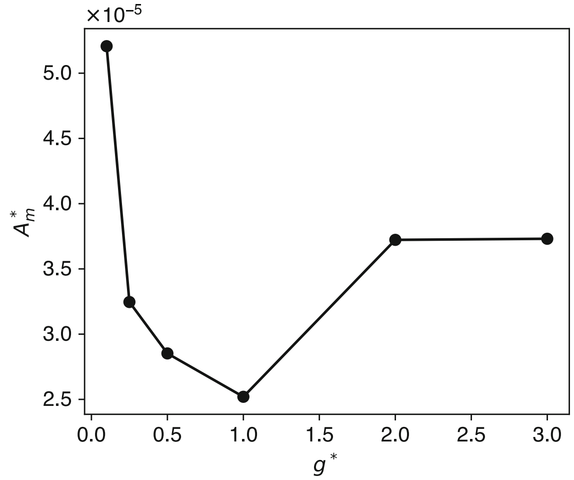

Fig. 3 Variation of the mean peak-to-peak amplitude with g^*

3.3 Two coupled oscillators

Finite element simulations of the two-oscillator system were carried out for the same flow and boundary conditions as for the single oscillator system. The system was simulated for $g^* = 0.10, 0.25, 0.50, 1.00, 2.00$, and 3.00, so that the cases from close spacing to large spacing are covered.

3.3.1 Oscillator response

The effect of g^* on the response of the oscillator is shown in Fig. 3. The mean peak-to-peak amplitude of the displacement response A_m^* is plotted against g^*. For

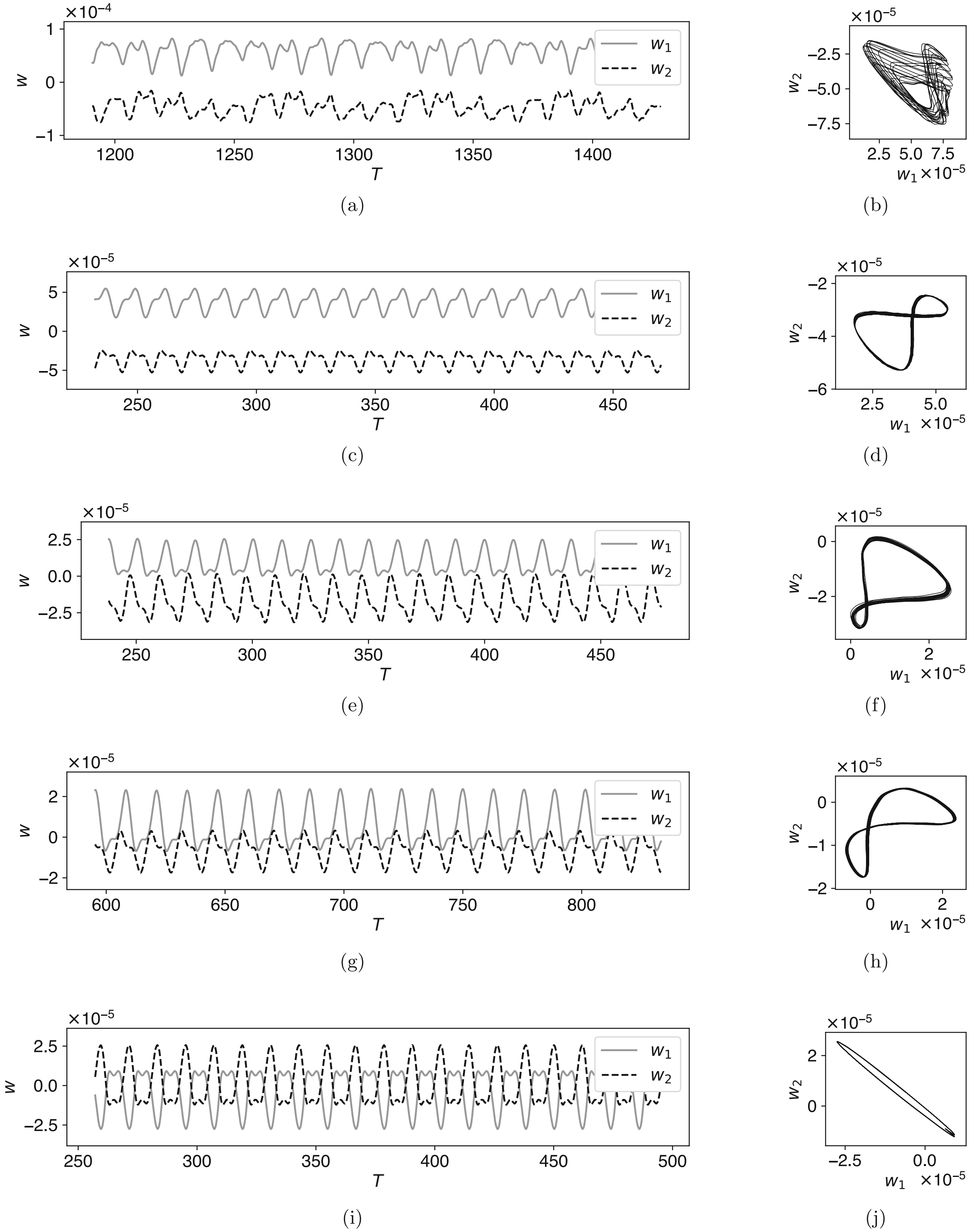

(a)

(b)

(c)

(d)

(e)

(f)

(g)

(h)

(i)

(j)

Fig. 4 Time histories for $g^* = 0.10$, $g^* = 0.25$, $g^* = 0.50$, $g^* = 1.00$ and $g^* = 2.00$ in (**a**), (**c**), (**e**), (**g**), and (**i**), respectively, and corresponding Lissajous plots in (**b**), (**d**), (**f**), (**h**), and (**j**)

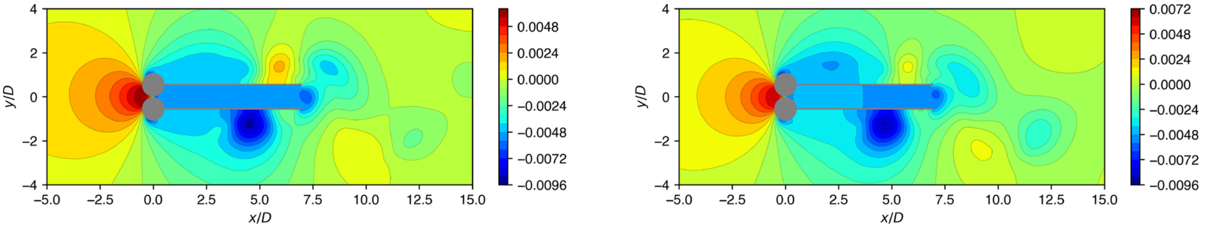

(a) w_1 maximum (b) w_2 maximum

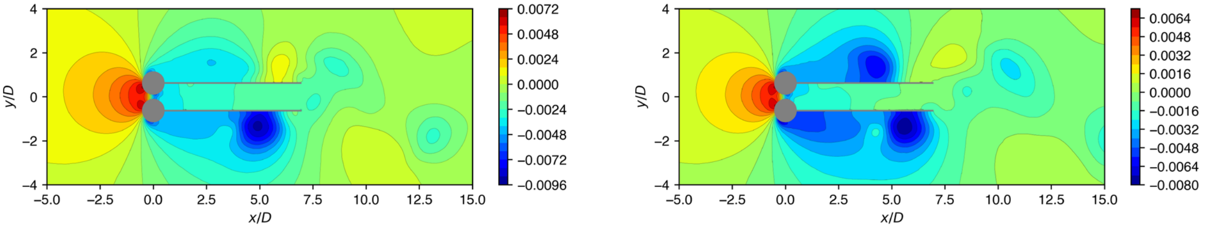

(c) w_1 maximum (d) w_2 maximum

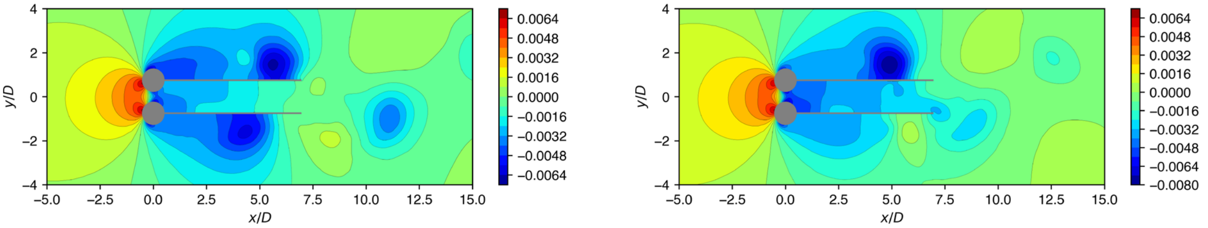

(e) w_1 maximum (f) w_2 maximum

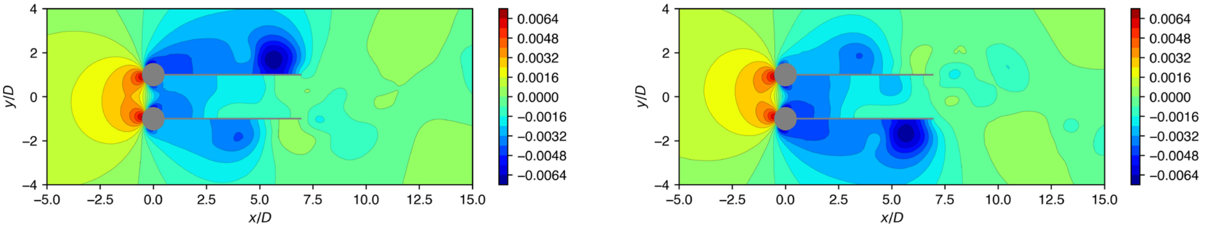

(g) w_1 maximum (h) w_2 maximum

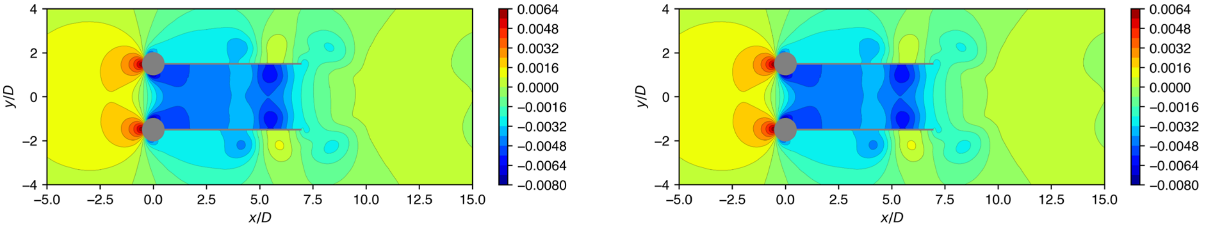

(i) w_1 maximum (j) w_2 maximum

Fig. 5 Pressure contours at the instant of maximum response for various g^* values: **a**, **b** for $g^* = 0.10$; **c**, **d** for $g^* = 0.25$; **e**, **f** for $g^* = 0.50$; **g**, **h** for $g^* = 1.00$; and **i**, **j** for $g^* = 2.00$

$g^* > 2.00$, the amplitude of the response approaches the corresponding response for an isolated oscillator. In the range $0.25 < g^* < 2.00$, the two-oscillator system is found to have a lower response amplitude compared to that of an isolated single oscillator. The minimum amplitude is observed for $g^* = 1.00$. For very small g^*, that is, $g^* \leq 0.25$, an amplified response is obtained. These results align with the experimental findings of Azadeh-Ranjbar et al. [27], demonstrating that the oscillator power output, which is dependent on oscillation amplitude, initially decreases and then increases as g^* decreases.

The time histories and phase plane plots for the responses obtained for various g^* are plotted in Fig. 4. For $g^* > 2.00$, the response is out of phase as the configuration space plot is nearly a straight line with a negative slope. As g^* is reduced, the response becomes asymmetric, and for $g^* = 0.10$, the response is aperiodic and a beating charateristic is noted. In all cases, the two oscillators vibrate over a nonzero mean value. The pressure contours at the instant of maximal response for various g^* values are shown in Fig. 5.

From the PSD plots shown in Fig. 6, it can be concluded that for $g^* = 0.10$, there is a fundamental frequency $f_1^* = 0.08$ and the higher harmonics $f_2^* = 2f_1^*$ and $f_3^* = 3f_1^*$. There is also another secondary frequency $f_s^* = 0.017$. There are tertiary frequencies that arise out of interaction between the higher harmonics and mode s. These tertiary modes have the frequencies $f_n^* \pm f_s^*$. The fundamental frequencies for various g^* are given in Table 2. For $g^* = 0.25$, $g^* = 0.50$, $g^* = 1.00$, and $g^* = 2.00$, only the higher harmonics are present. The algorithm from Eckmann et al. [36] was used to compute the Lyapunov exponents for the displacement response time series by using the `nolds` python package. For $g^* = 0.1$, the determined Lyapunov exponents were small but positive, suggesting a chaotic nature of the oscillations.

3.3.2 Vorticity contours

The vorticity contours for the two-oscillator case are shown in Fig. 7. There is no vortex shedding from the sides facing each other for the $g^* = 0.10$ case due to the *near wall effect* [15]. Collectively, the two oscillators behave like a single bluff body. The gap flow is parallel to the direction of the flow. Vorticity contours also suggest that there is a bias in the flow direction in the two-oscillator case for intermediate spacing, as shown

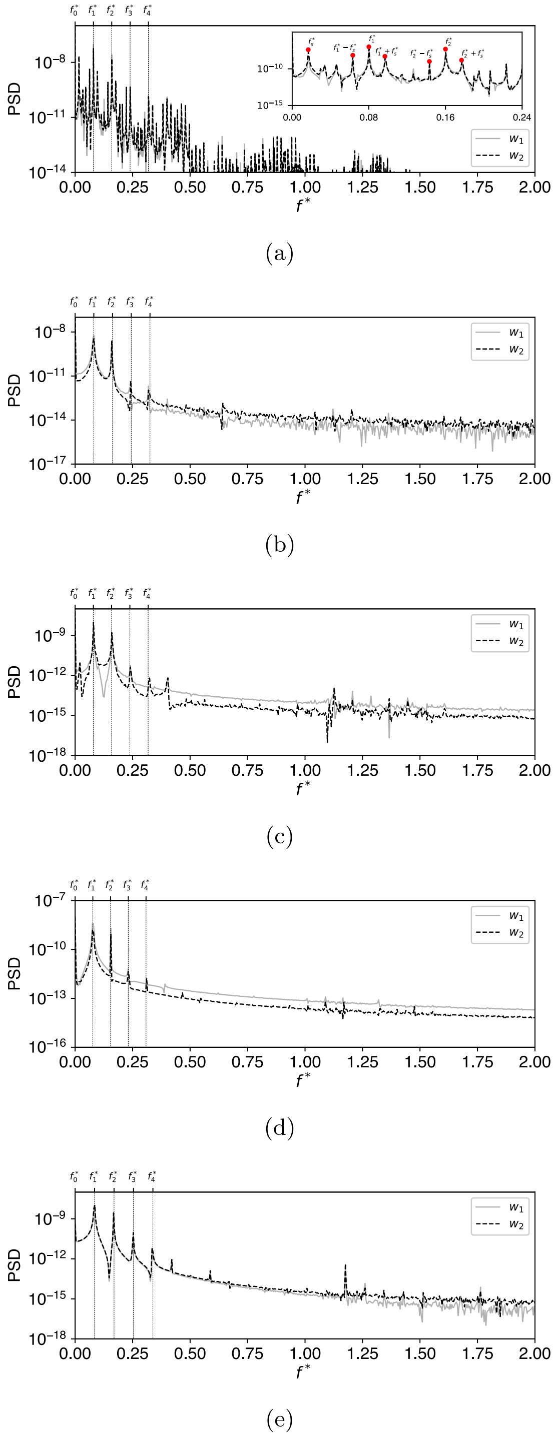

(a)

(b)

(c)

(d)

(e)

Fig. 6 PSDs of the oscillator displacement responses for various g^*: **a** $g^* = 0.10$, **b** $g^* = 0.25$, **c** $g^* = 0.50$, **d** $g^* = 0.1$, and **e** $g^* = 2.00$. Peaks at harmonics of vortex shedding frequencies (f_n^*) as well as the sidebands, corresponding to tertiary modes ($f_n^* \pm f_s^*$) are marked in the inset

Table 2 Frequencies of oscillation for various g^*

g^*	f_1^*	f_2^*	f_3^*
0.10	0.080	0.160	0.241
0.25	0.081	0.160	0.239
0.50	0.079	0.159	0.239
1.00	0.077	0.155	0.231
2.00	0.084	0.168	0.252

in Figs. 7b, c, d. This is due to the fact that the oscillators are in the biased flow regime as described in earlier work [37]. The asymmetrical flow gap is characterized by a gap flow biased towards one of the cylinders. The cylinder towards which the flow is biased has a narrow near wake, a higher vortex shedding frequency, and a higher drag coefficient in contrast to the other cylinder, which has a wider near wake, a lower vortex shedding frequency, and a lower drag coefficient [10]. For $g^* = 2.00$ and higher, the vorticity contours are antisymmetric mirror reflections of each other about the x-axis.

3.3.3 Proper orthogonal decomposition and dynamic mode decomposition of pressure fields

Proper Orthogonal Decomposition has been used to get the pressure POD modes for $g^* = 0.10$, $g^* = 1.00$, and $g^* = 2.00$. From the POD algorithm, the dominant modes are obtained based on energy contributions. The POD modes and the mode spectra are shown in Figs. 8, 9, and 10. The power spectra of the POD modes involve multiple peaks, revealing contributions from other uncorrelated modes. Multiple modes for the same dominant frequency are obtained. As the spacing is varied, one can note that the different POD modes have a symmetric character in the transverse direction for the large spacing case, and this symmetric character is lost as one moves to the closest spacing case. In addition, one can also see how the spectral character changes across the different modes for a given spacing as well as how this character changes with respect to the spacing. For the large spacing cases, the spectral characteristics for a particular mode are found to have qualitative similarities.

Dynamic Mode Decomposition is used to get the DMD modes for the pressure field for $g^* = 0.10,\ 1.00$, and 2.00. The results can be used to examine the spa-

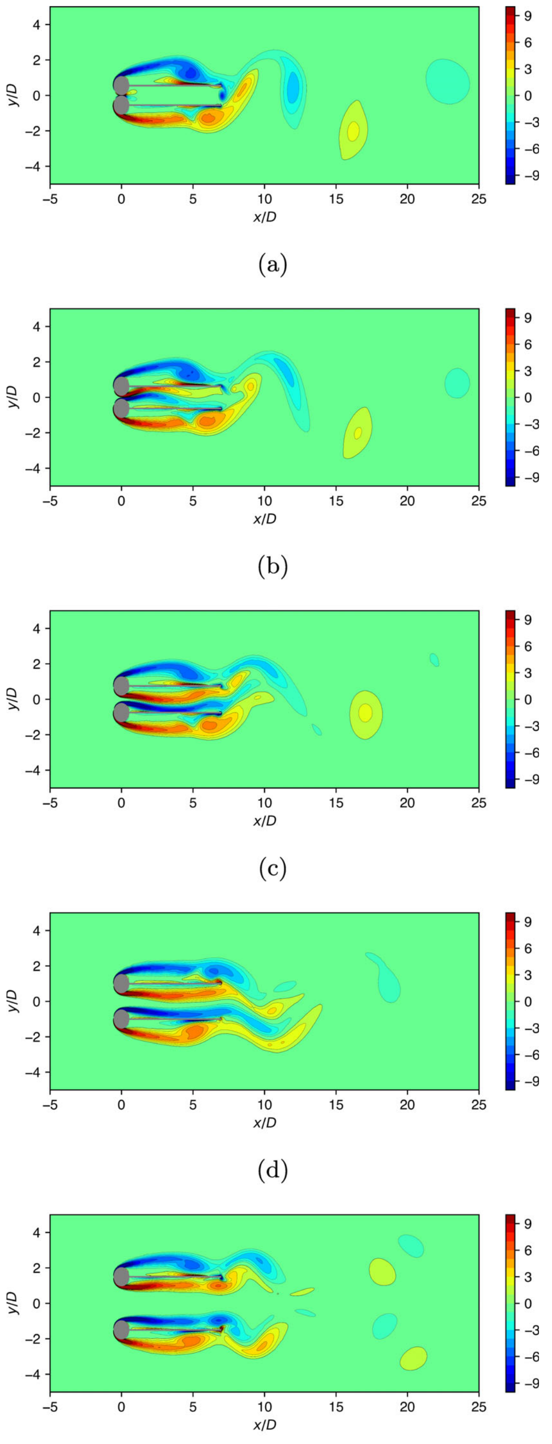

(a)

(b)

(c)

(d)

(e)

Fig. 7 Vorticity contours: **a** $g^* = 0.10$, **b** $g^* = 0.25$, **c** $g^* = 0.50$, **d** $g^* = 1.00$, and **e** $g^* = 2.00$. In this plot and similar plots that follow, the positive values correspond to counterclockwise rotation and the negative values correspond to clockwise rotation

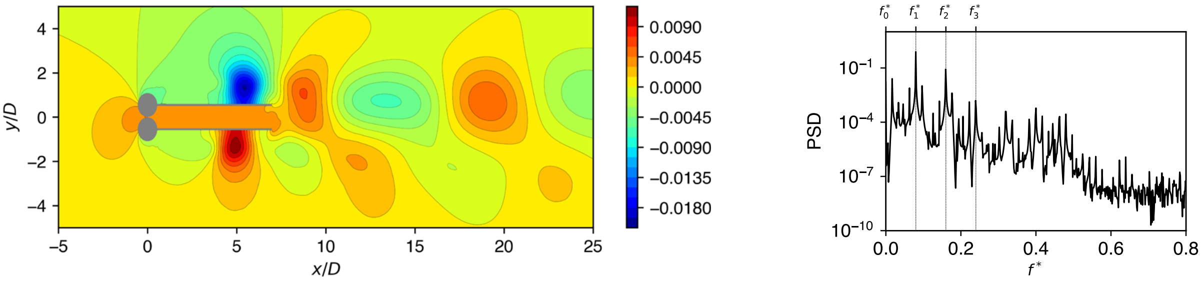

(a) POD Mode 1 (b) POD Mode 1 spectrum

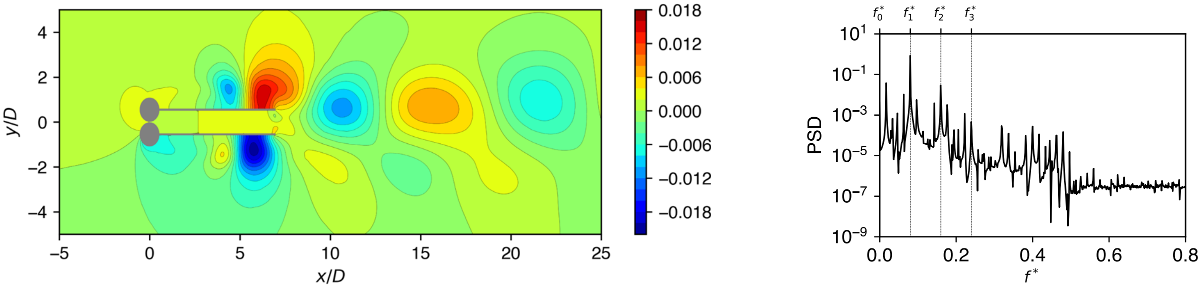

(c) POD Mode 2 (d) POD Mode 2 spectrum

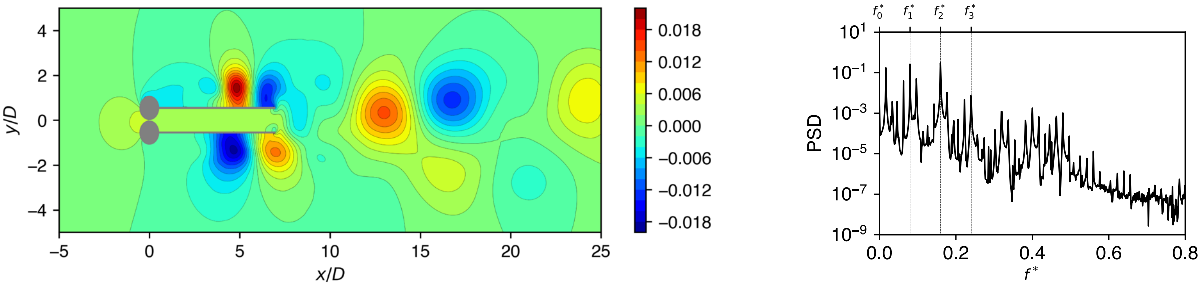

(e) POD Mode 3 (f) POD Mode 3 spectrum

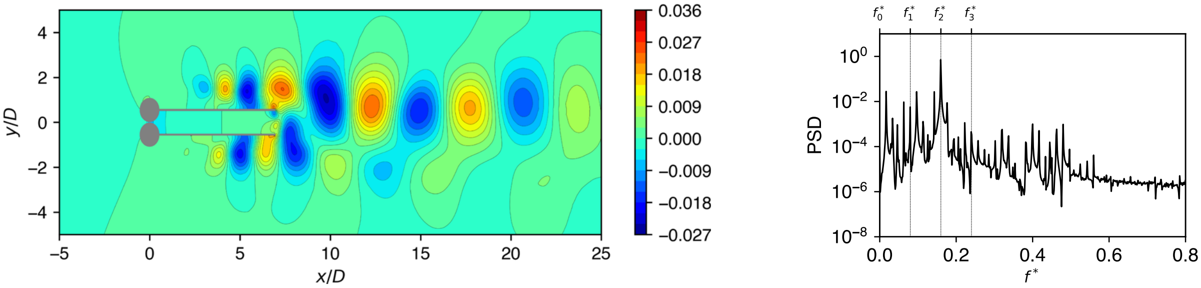

(g) POD Mode 4 (h) POD Mode 4 spectrum

Fig. 8 Pressure POD modes and mode spectra for $g^* = 0.10$

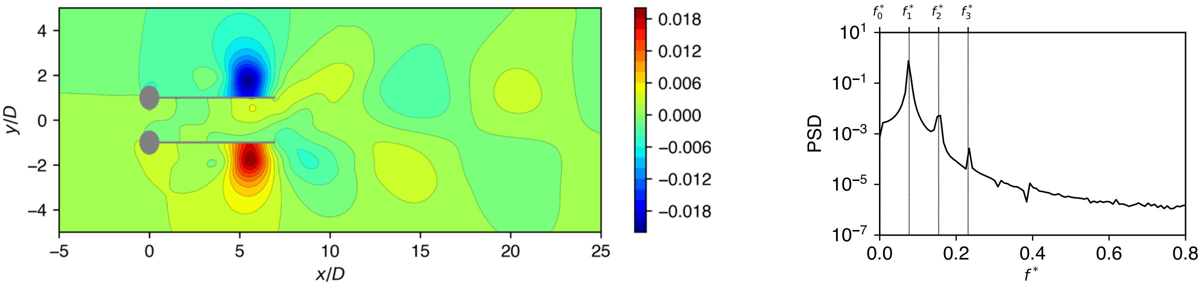

(a) POD Mode 1 (b) POD Mode 1 spectrum

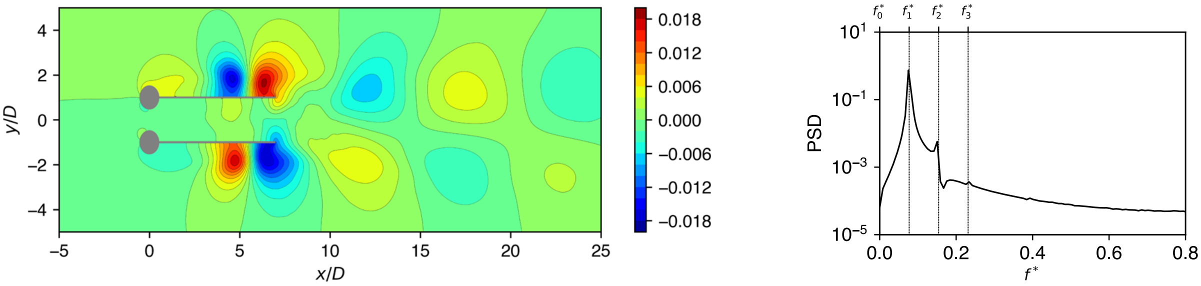

(c) POD Mode 2 (d) POD Mode 2 spectrum

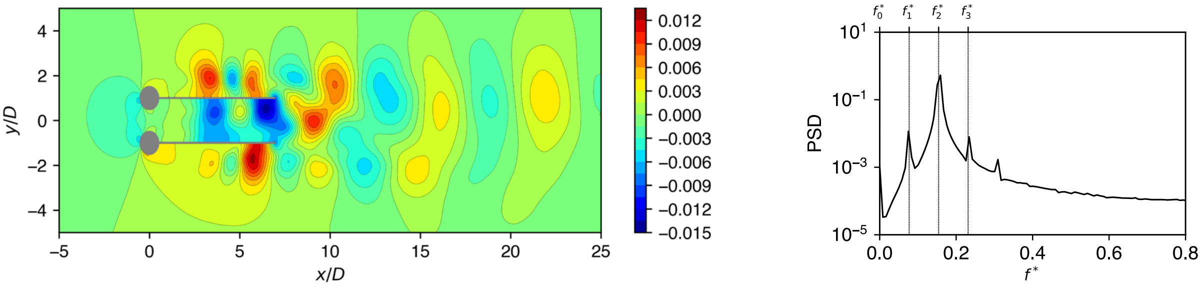

(e) POD Mode 3 (f) POD Mode 3 spectrum

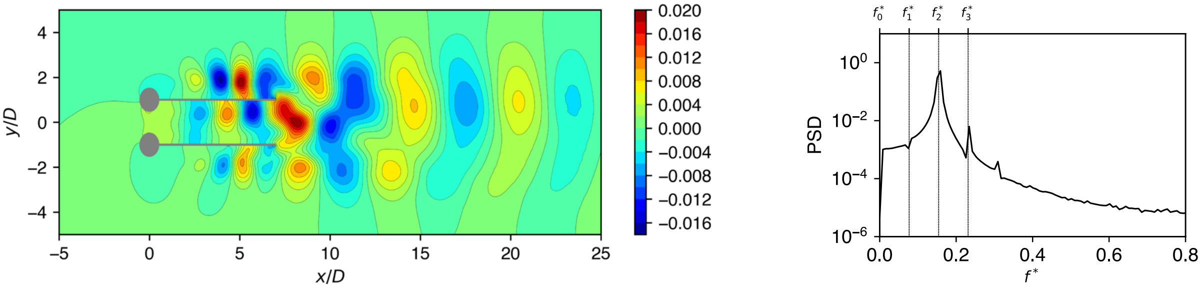

(g) POD Mode 4 (h) POD Mode 4 spectrum

Fig. 9 Pressure POD modes and mode spectra for $g^* = 1.00$

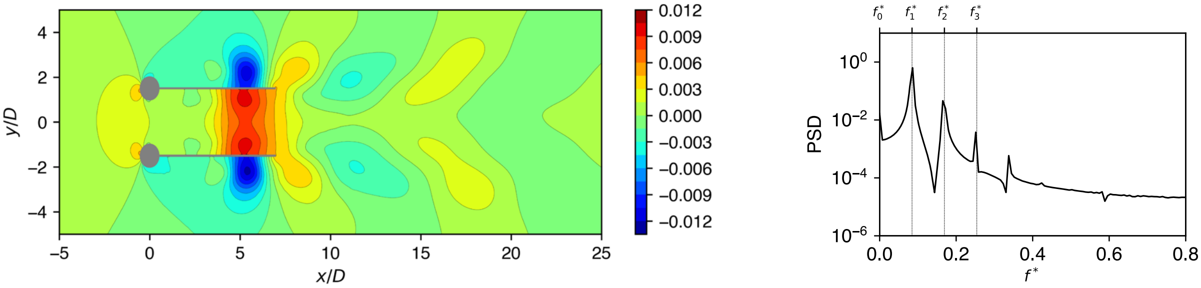

(a) POD Mode 1 (b) POD Mode 1 spectrum

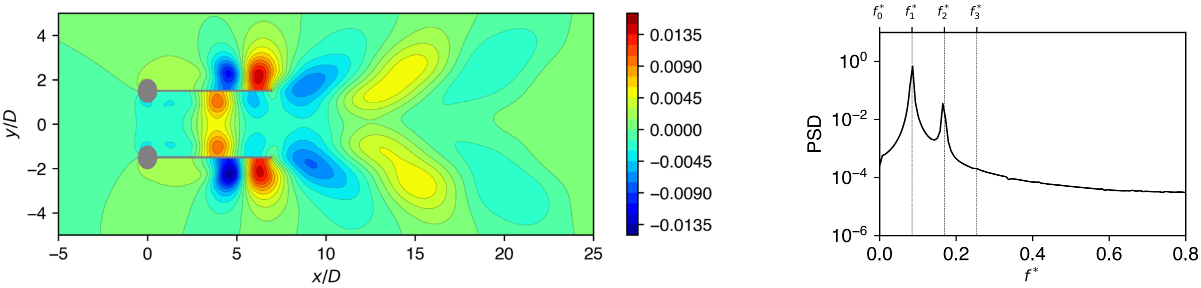

(c) POD Mode 2 (d) POD Mode 2 spectrum

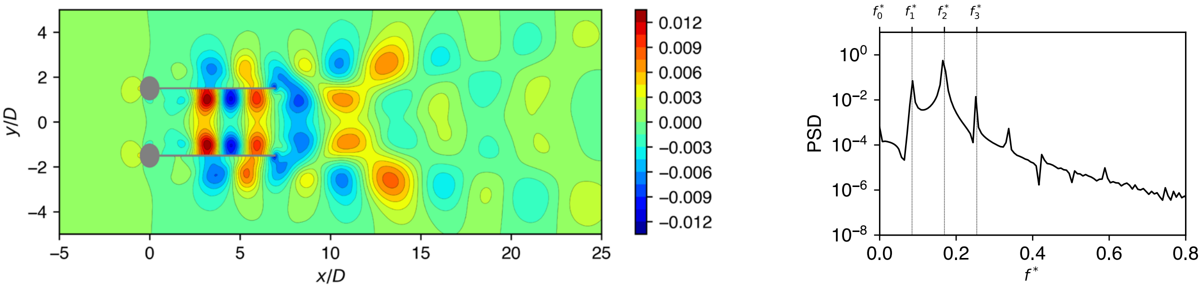

(e) POD Mode 3 (f) POD Mode 3 spectrum

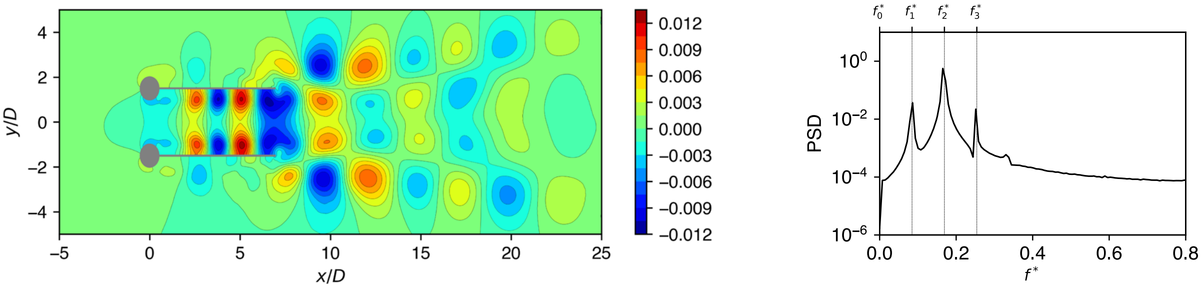

(g) POD Mode 4 (h) POD Mode 4 spectrum

Fig. 10 Pressure POD modes and mode spectra for $g^* = 2.00$

Table 3 Frequencies of DMD modes of the pressure field for various g^*

g^*	f_1^{DMD}	f_2^{DMD}	f_3^{DMD}	f_4^{DMD}
0.10	0.0799	0.1598	0.0170	0.0969
1.00	0.0776	0.1553	0.2329	0.3106
2.00	0.0839	0.1678	0.2518	0.3357

tiotemporally coherent modes of the fluid system. The frequencies of various modes obtained from the DMD analysis are arranged in decreasing order of modal amplitude and presented in Table 3. The mean mode with zero frequency is excluded here. From the modes, a strong connection between the DMD modes and the peaks in the PSD of the oscillator response can be noted. The pressure DMD modes for $g^* = 0.10$, $g^* = 1.00$, and $g^* = 2.00$ are shown in Figs. 11, 12, and 13, respectively. For $g^* = 1.00$ and $g^* = 2.00$, the DMD modes correspond to the fundamental frequency f_1^* and the higher harmonics. However, for $g^* = 0.10$, a low-frequency secondary mode, corresponding to the frequency f_s^*, is found to emerge. This frequency corresponds to the beating phenomenon observed in the oscillator response for $g^* = 0.10$. The tertiary modes again have the frequencies $f_n^* \pm f_s^*$. For the largest transverse spacing, the higher DMD modes have a symmetric character in the transverse direction. This symmetric character is lost as the transverse spacing is decreased. This is influenced by the coupling between the wakes shed from the oscillating bodies.

3.3.4 Effect of splitter plate addition

To analyze the effect of the addition of splitter plates at the Reynolds number used for the study, the flow over stationary side-by-side cylinders was simulated

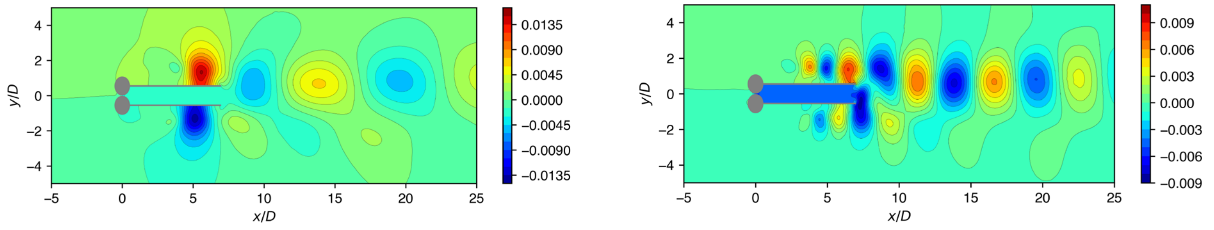

(a) Mode 1 (b) Mode 2

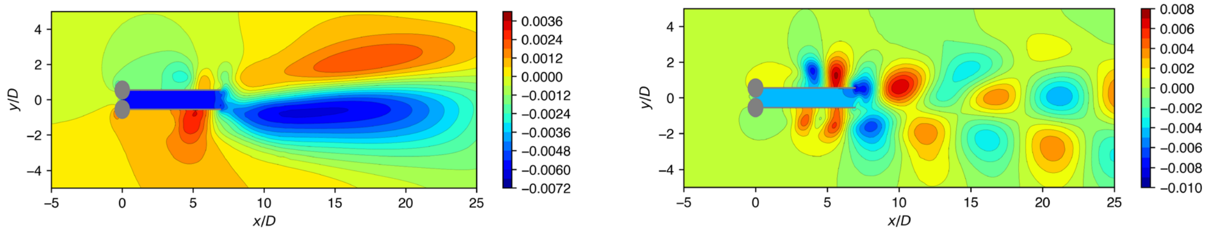

(c) Mode 3 (d) Mode 4

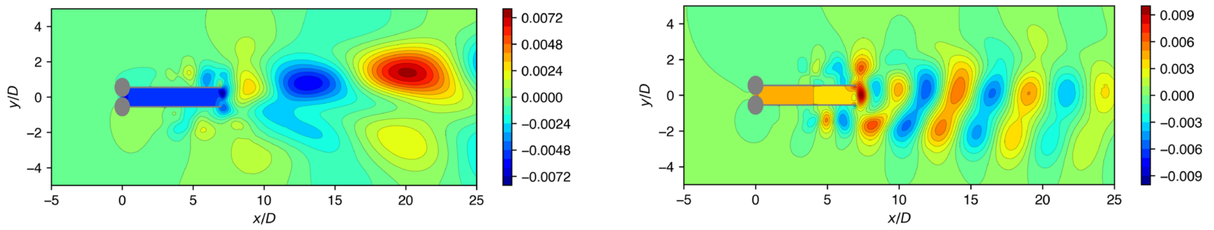

(e) Mode 5 (f) Mode 6

Fig. 11 Pressure DMD modes for $g^* = 0.10$

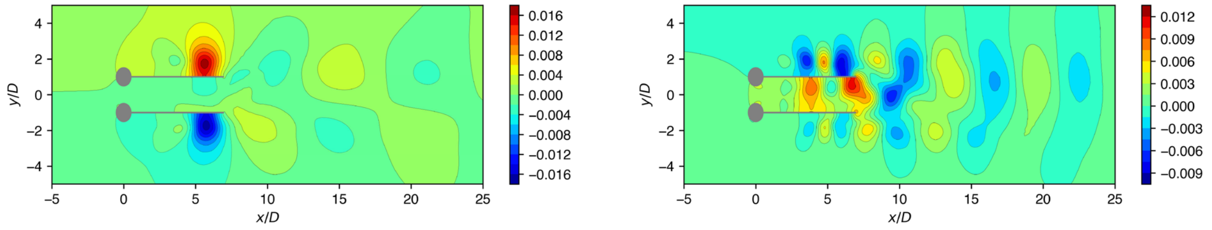

(a) Mode 1 (b) Mode 2

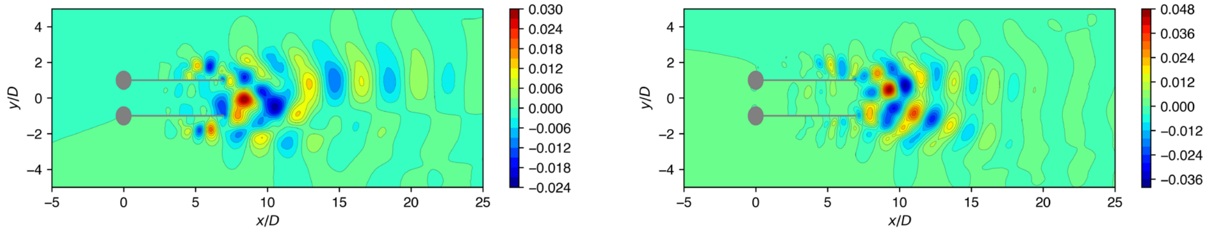

(c) Mode 3 (d) Mode 4

Fig. 12 Pressure DMD modes for $g^* = 1.00$

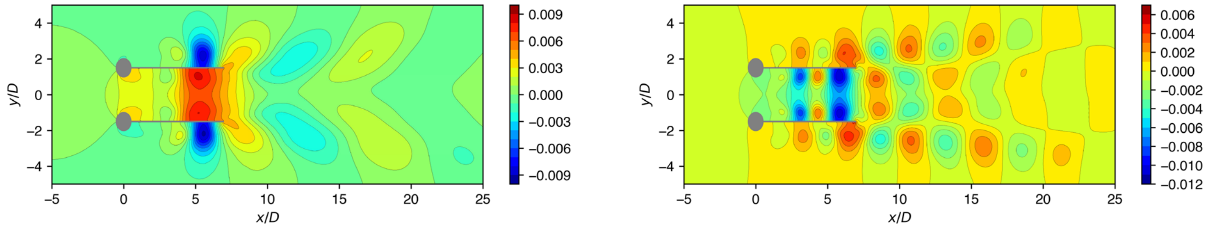

(a) Mode 1 (b) Mode 2

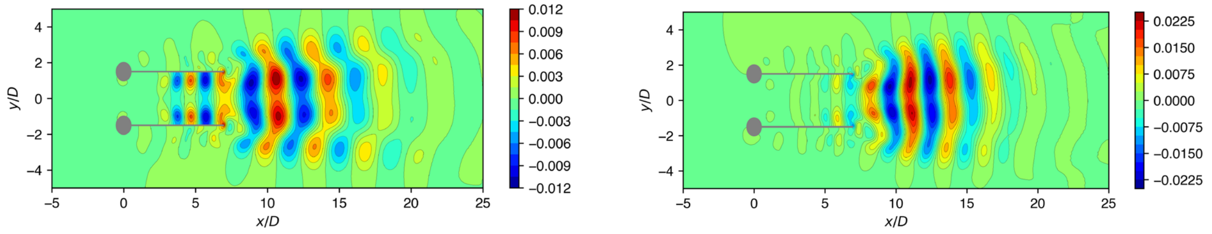

(c) Mode 3 (d) Mode 4

Fig. 13 Pressure DMD modes for $g^* = 2.00$

for $g^* = 0.10$, 1.00, and 2.00. The vorticity contours are shown in Fig. 14. For $g^* = 2.00$, the dominant vortex shedding frequency is $f^*_{vs} = 0.20$, which is close to the vortex shedding frequency of an isolated cylinder. The vortex shedding is anti-symmetric. For $g^* = 1.00$, $f^*_{vs} = 0.20$, and flip-flopping is observed. For $g^* = 0.10$, the two cylinders collectively behave like a single bluff body with a vortex shedding frequency $f^*_{vs} = 0.11$, which is half of the vortex shedding frequency obtained for an isolated cylinder. Since for a particular Strouhal number, the vortex shedding frequency is inversely proportional to the diameter of the cylinder, for a bluff body with twice the characteristic length of a reference bluff body, vortices will

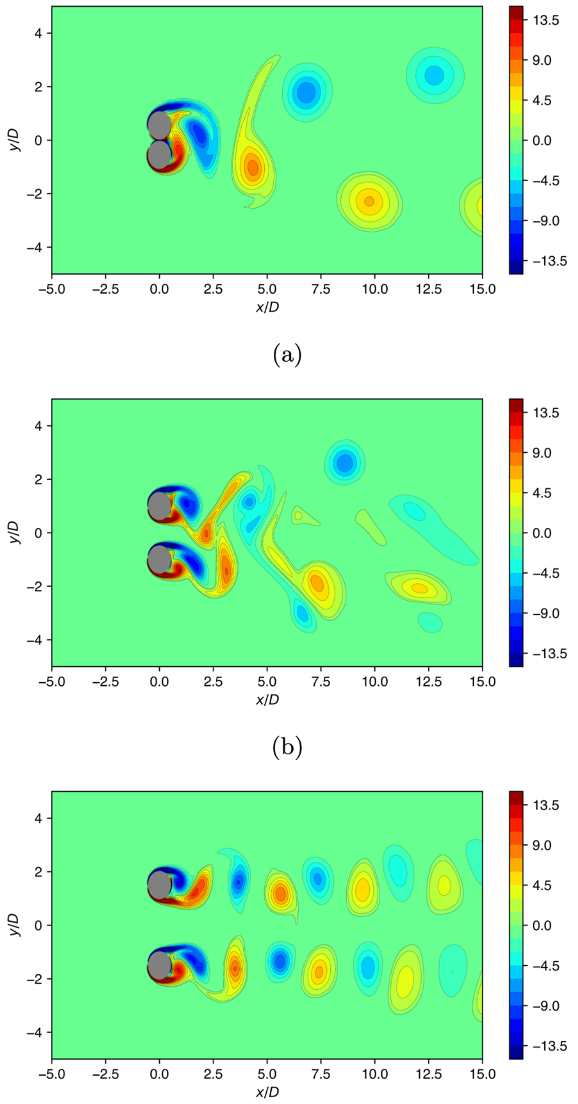

(a)

(b)

(c)

Fig. 14 Vorticity contours for cylinders without beams: **a** $g^* = 0.10$, **b** $g^* = 1.00$, and **c** $g^* = 2.00$

be shed at half the frequency of that for the reference bluff body. Hence, it can be concluded that for two cylinders in close proximity, vortices are shed like that for a single bluff body with twice the diameter of the original bluff body. Additionally, the flow over the two-oscillator system with rigid beams was simulated for $g^* = 0.10$. DMD was used to obtain the modes and modal frequencies, which were found to be identical to those of the system with elastic beams, suggesting that the fluid dynamics is dominant in the system response in both cases. The addition of splitter plates is found to reduce the vortex shedding frequency.

4 Concluding remarks

In this work, the authors have considered bluff-body oscillators in the form of a cylinder attached to a cantilever and created a finite element model for a single bluff-body oscillator and coupled bluff-body oscillators. These computational models have been used to study the associated fluid–structure interactions. For the case of two bluff-body oscillators, the variation in the system response with respect to the transverse spacing (g^*) has been examined, and it is found that with a decrease in g^*, the mean amplitude of the oscillations is found to first decrease and then increase as g^* tends to zero. This is the first computational confirmation of the experimental trend observed in earlier work [27].

Dynamic mode decomposition has been used to extract spatiotemporal coherent modes from the pressure field. These modes corresponded to the peaks in the power spectrum of the oscillator response. Apart from dynamic mode decomposition, proper orthogonal decomposition has also been used to study the system response characteristics. For close transverse spacing, it is found the oscillator response can be aperiodic. As the spacing is increased, for the largest spacing, the determined modes are found to have spatial symmetry in the transverse direction. These studies help to understand how the transverse spacing between the cylinder-cantilever bluff-body oscillators influences the vortical structures and the resulting vortex-induced oscillations. Additionally, insights have been gained into specific spatial modes that dominate the dynamics and how the mode participation changes with respect to different parameters. The findings of this research provide a computational foundation for building models of coupled bluff-body oscillators and optimizing configurations of arrays of these oscillators for enhanced energy harvesting efficiency.

Acknowledgements Partial support received for this work by B. Balachandran of the University of Maryland, College Park, USA through the U.S. National Science Foundation through Grant No. CMMI2131594 is gratefully acknowledged.

Funding Support received for this work has been acknowledged.

Code availability The algorithms used for the data analysis are included in the paper. Details related to the use of the commercial code Abaqus have been provided in the appendices.

Declarations

Conflict of interest The authors declare that they have no Conflict of interest.

Appendix A FSI methodology

Due to the strong coupling between fluid and structural motions, especially, in the case of multiple oscillators, a fully coupled fluid–structure interaction (FSI) modeling scheme is employed. The FSI problem is implemented by using the Finite Element package Abaqus [29]. The model involves an incompressible Newtonian fluid flow interacting with an elastic solid undergoing large deformations.

In Abaqus, a sequentially coupled scheme is utilized with non-overlapping computational domains for the fluid (Ω_f) and structural (Ω_s) regions. A conforming interface (Γ_I) is utilized to maintain continuity and facilitate interaction between the fluid and structural domains, as illustrated in Fig. 15. The structural solver is used to determine the motions of the structure, track the movement of the fluid boundary, and enforce velocity boundary conditions to facilitate the interaction between the fluid and structural domains. The fluid solver is used to calculate the velocity and pressure fields in the fluid domain. The resulting force on the boundary is transferred as an external force to the structural domain in the subsequent time step. A body-fixed Lagrangian mesh is chosen for the structure to accurately capture the structure's deformation, whereas a space-fixed Eulerian mesh is used for fluid modeling due to the associated ability for effectively handling large deformations. The motions of the structure induce changes in the interface (Γ_I), leading to distortions in the fluid boundary mesh as a result of the dynamic interactions between the fluid and solid domains. In Abaqus, the Arbitrary Lagrangian Eulerian (ALE) approach is utilized to dynamically remesh the fluid domain, enabling the solution of governing equations on a moving mesh to accurately capture the fluid–structure interaction dynamics.

The material point displacement $\mathbf{u}^s$ in the structure is derived from the momentum equation expressed in the Lagrangian description as follows:

$$\rho^s \ddot{\mathbf{u}}^s - \nabla \cdot (J \sigma^s F^{-\top}) + \mathbf{b}^s = \mathbf{0} \quad \text{in } \Omega_s \tag{A1}$$

Here, σ^s is the Cauchy stress, $F = I + \nabla \mathbf{u}^s$ is the deformation gradient tensor, and J is the determinant of F.

Linear elastic material behavior and geometrically nonlinear deformation are captured by using the St. Venant-Kirchhoff constitutive law:

$$\sigma^s = \frac{1}{J} F (\lambda^s \operatorname{tr}(E) I + 2\mu^s E) F^\top \tag{A2}$$

where $E = \frac{1}{2}(F^\top F - I)$, and λ^s and μ^s are the Lamé constants.

The velocity field $\mathbf{v}^f$ in the fluid domain is obtained by using the Navier–Stokes equation, written in the Eulerian description as follows:

$$\rho^f \frac{\partial \mathbf{v}^f}{\partial t} + \mathbf{v}^f \cdot \nabla \mathbf{v}^f - \nabla \cdot \sigma^f + \mathbf{b}^f = \mathbf{0} \quad \text{in } \Omega_f \tag{A3}$$

Here, ρ^f is the fluid density, $\mathbf{b}^f$ is the body force, and σ^f is the fluid stress.

The fluid is considered to exhibit Newtonian behavior, which results in the equation

$$\sigma^f = -pI + \eta(\nabla \mathbf{v}^f + \nabla \mathbf{v}^{f\top}) \tag{A4}$$

where p is the thermodynamic pressure and η is the dynamic viscosity.

The fluid is considered to be incompressible, and hence, the Pressure-Poisson equation is used to determine the pressure from the velocity field by using

$$\nabla^2 p = -\nabla \mathbf{v}^f : \nabla \mathbf{v}^f \tag{A5}$$

Displacement and traction continuity at the interface are maintained by using the following conditions:

$$\begin{aligned} \mathbf{v}^f \Big|_{\Gamma_f} &= \frac{d\mathbf{u}^s}{dt}\Big|_{\Gamma_s} \\ \boldsymbol{\sigma}^f : \mathbf{n}\Big|_{\Gamma_f} &= \boldsymbol{\sigma}^s : \mathbf{n}\Big|_{\Gamma_s} \end{aligned} \tag{A6}$$

Fig. 15 Sequential coupled FSI approach

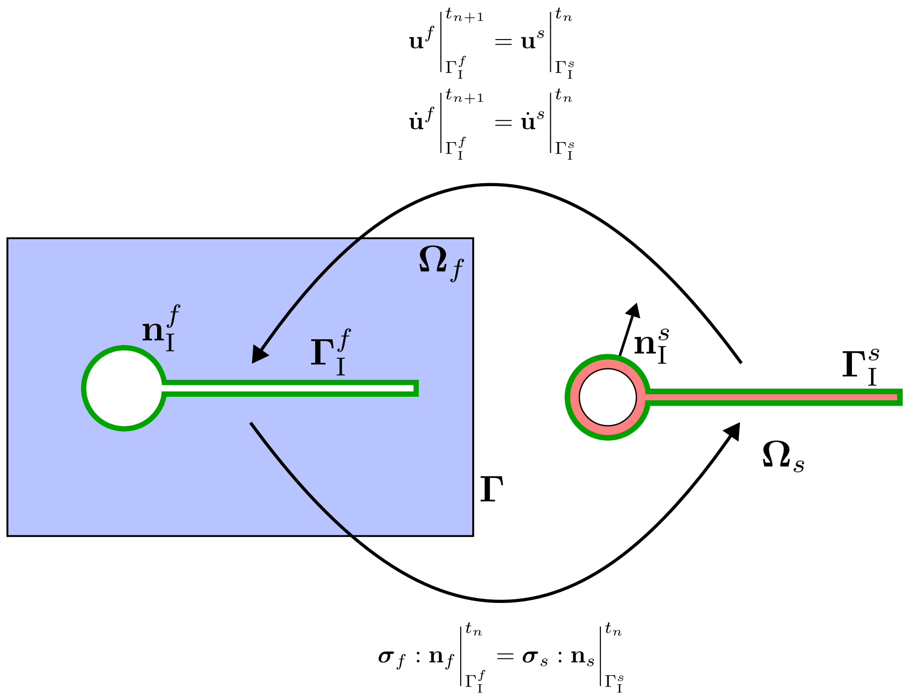

Appendix B Simulation and mesh parameters

Simulation parameters

Implicit dynamic simulation is conducted until a steady state is achieved. In order to solve the nonlinear equations for the structural response, the full Newton solution technique is used. Automatic time stepping is used, and the maximum CFL number is set to 0.5. The divergence tolerance is set to 1×10^{-10}. The Trapezoidal method is used for time integration of the fluid equations. This method is second-order accurate and A-stable.

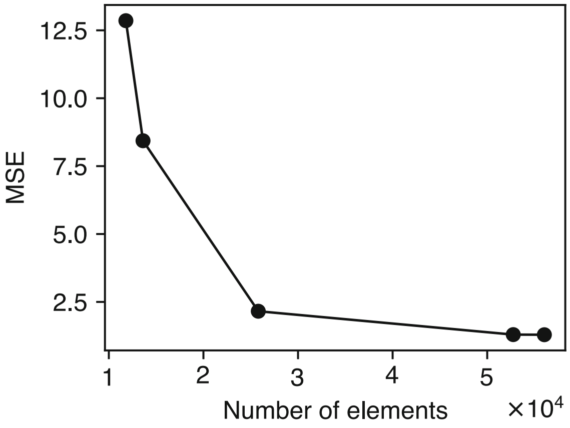

Fig. 16 Mean squared error in oscillator velocity response versus number of elements in the fluid domain

Mesh and mesh convergence

A structured mesh is used for the oscillator. For the fluid domain, a hybrid mesh with an unstructured part in the vicinity of the oscillator and a remaining structured part was created and used for all the models. The mesh was very fine, with an element size of 0.02 nondimensional length units in the proximity of the FSI interface. This mesh was gradually made coarser towards the domain boundaries, as shown in Fig. 17a. Mesh convergence and mesh independence studies were conducted to determine the optimal mesh size in the fluid domain. The system was simulated for a total of 15.00 s, and the finest mesh solution was assumed to be correct. The mean squared error in the velocity response is plotted against the number of elements in Fig. 16. The coarsest mesh that yielded acceptable results was identified from this plot. Further refinement beyond this point resulted in diminishing returns with a negligible improvement in accuracy. The mesh, which was depicted in Fig. 17a, was chosen as the optimal balance between computational efficiency and solution fidelity.

Fig. 17 Meshes used for simulation

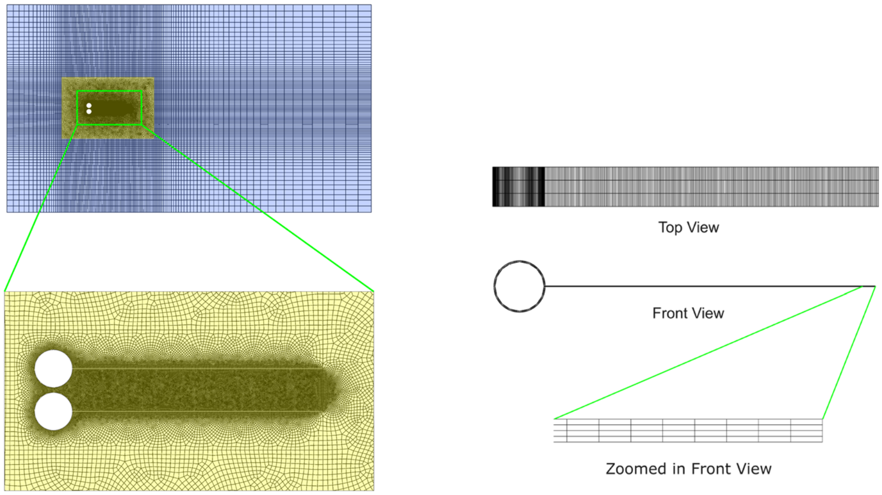

(a) Fluid domain mesh (Structured mesh highlighted in blue and unstructured mesh highlighted in yellow).

(b) Oscillator mesh.

To capture the variation in the bending stress accurately, the beam had four elements through the thickness of the cantilever, as shown in Fig. 17b. Arbitrary Lagrangian Eulerian (ALE) based adaptive meshing is employed to remesh the fluid domain at each time step. This enables the mesh nodes to be moved without changing the mesh topology. To successfully study fluid–structure interactions, the FSI boundary of the fluid and structure should match exactly. Since a 2D approximation is used, the model has a cylinder and beam of equal width. The 2D model of the oscillator necessitates having the cylinder length to be equal to the beam width. Hence, the mass of the cylinder is artificially increased in order to keep the oscillation frequency the same as in the original system. The 2D approximation also results in a flow field that is representative of the flow field over an infinite cylinder with a splitter plate attached throughout its length.

References

1. Luongo, A., Zulli, D., Piccardo, G.: Analytical and numerical approaches to nonlinear galloping of internally resonant suspended cables. J. Sound Vib. **315**(3), 375–393 (2008). https://doi.org/10.1016/j.jsv.2008.03.067
2. Nayfeh, A.H., Mook, D.T.: Nonlinear Oscillations. John Wiley & Sons, Weinheim (2008). https://doi.org/10.1002/9783527617586
3. Païdoussis, M.P.: Fluid-Structure Interactions: Slender Structures and Axial Flow, vol. 1. Academic press, San Diego (1998). https://doi.org/10.1016/C2011-0-08057-2
4. Dowell, E.H., Tang, D.: Nonlinear aeroelasticity and unsteady aerodynamics. AIAA J. **40**(9), 1697–1707 (2002). https://doi.org/10.2514/2.1853
5. Liu, L., Wong, Y.S., Lee, B.H.K.: Application of the centre manifold theory in non-linear aeroelasticity. J. Sound Vib. **234**(4), 641–659 (2000). https://doi.org/10.1006/jsvi.1999.2895
6. Vasconcellos, R., Abdelkefi, A.: Nonlinear dynamical analysis of an aeroelastic system with multi-segmented moment in the pitch degree-of-freedom. Commun. Nonlinear Sci. Numer. Simul. **20**(1), 324–334 (2015). https://doi.org/10.1016/j.cnsns.2014.05.017
7. Sumner, D.: Two circular cylinders in cross-flow: a review. J. Fluids Struct. **26**(6), 849–899 (2010). https://doi.org/10.1016/j.jfluidstructs.2010.07.001
8. Zhou, Y., Mahbub Alam, M.: Wake of two interacting circular cylinders: a review. Int. J. Heat Fluid Flow **62**, 510–537 (2016). https://doi.org/10.1016/j.ijheatfluidflow.2016.08.008
9. Landweber, L.: Flow about a pair of adjacent, parallel cylinders normal to a stream: Theoretical analysis. Technical Report 485, David Taylor Model Basin (1942)
10. Spivack, H.M.: Vortex frequency and flow pattern in the wake of two parallel cylinders at varied spacing normal to an air stream. J. Aeronaut. Sci. **13**(6), 289–301 (1946). https://doi.org/10.2514/8.11375
11. Kim, H.J., Durbin, P.A.: Investigation of the flow between a pair of circular cylinders in the flopping regime. J. Fluid Mech. **196**, 431–448 (1988). https://doi.org/10.1017/S0022112088002769
12. Williamson, C.H.K.: Evolution of a single wake behind a pair of bluff bodies. J. Fluid Mech. **159**, 1–18 (1985). https://doi.org/10.1017/S002211208500307X
13. Bearman, P.W., Wadcock, A.J.: The interaction between a pair of circular cylinders normal to a stream. J. Fluid Mech. **61**(3), 499–511 (1973). https://doi.org/10.1017/S0022112073000832

14. Sumner, D., Wong, S.S.T., Price, S.J., Païdoussis, M.P.: Fluid behaviour of side-by-side circular cylinders in steady cross-flow. J. Fluids Struct. **13**(3), 309–338 (1999). https://doi.org/10.1006/jfls.1999.0205
15. Xu, S.J., Zhou, Y., So, R.M.C.: Reynolds number effects on the flow structure behind two side-by-side cylinders. Phys. Fluids **15**(5), 1214–1219 (2003). https://doi.org/10.1063/1.1561614
16. Bai, X.-D., Zhang, W., Wang, Y.: Deflected oscillatory wake pattern behind two side-by-side circular cylinders. Ocean Eng. **197**, 106847 (2020). https://doi.org/10.1016/j.oceaneng.2019.106847
17. Williamson, C.H.K., Govardhan, R.: Vortex-induced vibrations. Ann. Rev. Fluid Mech. **36**, 413–455 (2004). https://doi.org/10.1146/annurev.fluid.36.050802.122128
18. Cossu, C., Morino, L.: On the instability of a spring-mounted circular cylinder in a viscous flow at low reynolds numbers. J. Fluids Struct. **14**(2), 183–196 (2000). https://doi.org/10.1006/jfls.1999.0261
19. Singh, S.P., Mittal, S.: Vortex-induced oscillations at low reynolds numbers: hysteresis and vortex-shedding modes. J. Fluids Struct. **20**(8), 1085–1104 (2005). https://doi.org/10.1016/j.jfluidstructs.2005.05.011
20. Roshko, A.: On the drag and shedding frequency of two-dimensional bluff bodies. Technical Note 3169, National Advisory Committee for Aeronautics, Washington (1954)
21. Kwon, K., Choi, H.: Control of laminar vortex shedding behind a circular cylinder using splitter plates. Phys. Fluids **8**(2), 479–486 (1996). https://doi.org/10.1063/1.868801
22. Akaydin, H.D., Elvin, N., Andreopoulos, Y.: Wake of a cylinder: a paradigm for energy harvesting with piezoelectric materials. Exp. Fluids **49**, 291–304 (2010). https://doi.org/10.1007/s00348-010-0871-7
23. Akaydin, H.D., Elvin, N., Andreopoulos, Y.: The performance of a self-excited fluidic energy harvester. Smart Mater. Struct. **21**(2), 025007 (2012). https://doi.org/10.1088/0964-1726/21/2/025007
24. Dai, H., Abdelkefi, A., Wang, L.: Theoretical modeling and nonlinear analysis of piezoelectric energy harvesting from vortex-induced vibrations. J. Intell. Mater. Syst. Struct. **25**(14), 1861–1874 (2014). https://doi.org/10.1177/1045389X14538329
25. Facchinetti, M.L., de Langre, E., Biolley, F.: Coupling of structure and wake oscillators in vortex-induced vibrations. J. Fluids Struct. **19**(2), 123–140 (2004). https://doi.org/10.1016/j.jfluidstructs.2003.12.004
26. Bellei, A., Balachandran, B.: Bluff body, piezoelastic oscillator: reduced-order model, vortex-induced vibrations, and energy harvesting. In: Proceedings of the ASME 2024 International Design Engineering Technical Conferences and Computers and Information in Engineering Conference (IDETC/CIE2024), Washington (2024). ASME
27. Azadeh-Ranjbar, V., Han, Y., Elvin, N., Andreopoulos, Y.: Non-linear piezoelectric fluidic energy harvesters: the mutual interaction of two oscillating cylinders. J. Intell. Mater. Syst. Struct. **31**(20), 2378–2389 (2020). https://doi.org/10.1177/1045389X20947178
28. Wani, K.Z., Pandey, M., Balachandran, B.: Coupled bluff body energy harvesters: vortex influenced dynamics. In: Proceedings of the IUTAM Symposium on Nonlinear Dynamics for Design of Mechanical Systems Across Different Length/Time Scales, Tsukuba, pp. 339–353 (2023)
29. Dassault Systémes: Abaqus 6.14 Documentation. (2015)
30. Roccia, B., Preidikman, S., Balachandran, B.: Computational dynamics of flapping wings in hover flight: a co-simulation strategy. AIAA J. **55**(6), 1806–1822 (2017). https://doi.org/10.2514/1.J055137
31. Luongo, A., Zulli, D.: Mathematical Models of Beams and Cables. John Wiley & Sons, Hoboken (2013). https://doi.org/10.1002/9781118577554
32. Lumley, J.L.: The structure of inhomogeneous turbulent flows. In: Atmospheric Turbulence and Radio Wave Propagation, 166–178 (1967)
33. Schmid, P.J.: Dynamic mode decomposition of numerical and experimental data. J. Fluid Mech. **656**, 5–28 (2010). https://doi.org/10.1017/S0022112010001217
34. Tu, J.H., Rowley, C.W., Luchtenburg, D.M., Brunton, S.L., Kutz, J.N.: On dynamic mode decomposition: theory and applications. J. Comput. Dyn. **1**(2), 391–421 (2014). https://doi.org/10.3934/jcd.2014.1.391
35. Demo, N., Tezzele, M., Rozza, G.: Pydmd: Python dynamic mode decomposition. J. Open Source Softw. **3**(22), 530 (2018). https://doi.org/10.21105/joss.00530
36. Eckmann, J.-P., Kamphorst, S.O., Ruelle, D., Ciliberto, S.: Liapunov exponents from time series. Phys. Rev. A **34**, 4971–4979 (1986). https://doi.org/10.1103/PhysRevA.34.4971
37. Mahbub Alam, M., Moriya, M., Sakamoto, H.: Aerodynamic characteristics of two side-by-side circular cylinders and application of wavelet analysis on the switching phenomenon. J. Fluids Struct. **18**(3), 325–346 (2003). https://doi.org/10.1016/j.jfluidstructs.2003.07.005